

Cite this: DOI: 00.0000/xxxxxxxxxx

Efficacy of simple continuum models for diverse granular intrusions

Shashank Agarwal^a, Andras Karsai^b, Daniel I Goldman^b, Ken Kamrin^{a*}Received Date
Accepted Date

DOI: 00.0000/xxxxxxxxxx

Granular intrusion is commonly observed in natural and man-made settings. Unlike single-phase media like solids and fluids, granular media can simultaneously display fluid-like and solid-like characteristics in a variety of intrusion scenarios. This trans-phase behavior increases the difficulty of accurately modeling these and other yielding (or flowable) materials. Micro-scale modeling methods, such as DEM (Discrete Element Method), capture this multiphase behavior by modeling the media at the grain scale, but interest often lies in the macro-scale characterizations of such systems. We examine the efficacy of a macro-scale continuum approach in modeling and understanding the physics and macroscopic phenomena behind a variety of granular intrusions cases using two basic frictional yielding constitutive models. We compare predicted granular force response and material flow to data in four 2D intrusion cases: (1) depth-dependence forces responses in horizontal submerged-intruder motion; (2) separation-dependent drag variation in parallel-plate vertical-intrusion; (3) initial-density-dependent drag fluctuations in free surface plowing, and (4) flow zone development in vertical plate intrusions in under-compacted granular media. Our continuum modeling approach captures the flow process and drag forces in each of these cases compared to experimental data while providing key meso- and macro-scopic insights. Our study highlights how continuum modeling approaches provide an alternative for efficient modeling as well as conceptual understanding of various granular intrusion phenomena.

1 Introduction

Granular intrusion is a common scenario in various natural and man-made situations^{1–3}. In many cases, the flow response to intrusion leads to a multi-phase behavior of the granular media, where the media shifts between solid-like, fluid-like, and gas-like states^{4,5}. This behavior depends on material properties and local state variables such as pressure and granular packing fraction⁶. The space and time dependence of these state variables, as well as the trans-phase behavior of the media, makes granular flow response challenging and computationally expensive to model.

Discrete Element Methods (DEM) are reliable and established methods for modeling granular media^{7,8}. In DEM, the granular medium is modeled at the particle level, with the frictional, elastic contact forces between adjacent and interacting particles obtained using standard contact models like Hertzian and Hookean contacts^{9,10}, generally with an assumption of no plastic yielding of the individual grains. The elastic and external forces are integrated via Newton's laws of motion to calculate particle ve-

locities and positions in DEM. In the past few decades, DEM has played a major role in the advancement of the field of granular media^{11,12}. However, the precision of DEM comes at a computational cost. Once the simulation's spatial scale becomes large relative to the size of the particles in the system, the computational cost of simulating many particles makes DEM prohibitively expensive. As an example, a 1mm particle diameter granular system with a 0.5m per side cubic domain would require evaluating $\sim 9 \times 10^8$ DOF per time step (at a packing fraction of 0.64 with 6 degrees of freedom, DOF per particle). While current large-scale granular DEM studies remain in the range of $\sim 10^7$ particles ($\sim 10^8$ DOF)^{13,14}, efforts are being made to extend this range. Most recently, some have reached the $\sim 10^9$ DOF range with the use of supercomputers and GPUs¹⁵.

In recent years, there has been a growing interest in modeling increasingly large granular systems, such as those relevant in ballistic impacts, wheeled locomotion, and agricultural plowing^{1–3,16,17}. This has led to a push for computationally faster alternatives to DEM, such as using continuum descriptions of granular media. At the fundamental level, cohesionless granular media can be described as a plastic material with a frictional yield criterion and no cohesion strength (hence no ability to sup-

^a 77 Massachusetts Ave, Cambridge, USA.^b North Ave NW, Atlanta, USA.

* E-mail: kkamrin@mit.edu

port tension). But, a comprehensive continuum model for fully describing a granular material requires incorporating a variety of behaviors shown by the media arising from the constituent grain shape, size, stiffness, distribution, and inter-particle interaction properties⁵, as well as effects due to the surrounding air (pressure and flow-drag) on the granular media¹⁸. Thus, often scenario-specific simplifications are made during constitutive model development. Conversely, even for a simple granular material, a constitutive framework encapsulating all granular phenomena would have to merge many different pieces together, e.g. collisional dynamics, by way of a dissipative kinetic theory^{19,20} in dilute regimes; strengthening based on packing fraction²¹ and internal state variables (like fabric and hysteresis) evolution²²; rate-dependence of the strength (such as $\mu(I)$ rheology²³); non-trivial yield surface shapes in stress space²⁴; and particle size effects^{25,26} in the dense flow regime.

A variety of efficient computational methods have been developed and utilized recently to aid in simulating continuum models for large deformation processes, such as the Material Point Method (MPM)^{27,28}, the Particle Finite Element Method (PFEM)²⁹, and Smoothed Particle Hydrodynamics (SPH)³⁰. In this regard, a recent study on high-speed locomotion of wheels³¹ in grains, a process which involves complex trans-phase characteristics of the soil and non-trivial grain motions, finds that a simple continuum treatment implemented with MPM captures the essential behaviors and agrees well with experimental data.

In this work, we highlight the capability of the continuum approach in modeling and explaining diverse granular intrusion phenomena using very basic constitutive ingredients. The phenomena we focus on herein have been independently studied in the literature, and our goal is to demonstrate that they can be quantitatively modeled and unified under a family of basic constitutive assumptions. We first introduce two constitutive representations of non-cohesive granular media: a non-dilatant plasticity model (NDPM), and a dilatant plasticity model (DPM). The DPM model permits dilatancy during dense flow while the NDPM model assumes dense flow is a constant-volume process (details later). Thus, the NDPM is suitable for modeling steady-state granular behaviors, while the DPM is a more suitable model for modeling transient flow processes. The latter is also a more elaborate model that converges to the former model under certain limits. Both of these models have their respective advantages depending on the scenarios they simulate. We do not include micro-inertial $\mu(I)$ effects (effects of grain-level inertia on material properties) in these models; thus both of these constitutive models are rate-insensitive.

We highlight the utility of each model by considering granular flow and force responses in four fundamental intrusion cases which have been studied in the literature: (1) depth-dependent force response in horizontal submerged intruder motion; (2) separation-dependent drag variation in parallel plate vertical intrusion; (3) initial density-dependent drag fluctuations in free surface plowing; and (4) flow zone development in vertical plate intrusions in undercompacted granular media (Figure 1). We use NDPM in the first two cases (which focus on a steady response), and DPM in the latter two cases (where transient effects are the

focus). Our continuum modeling approach captures the dynamics of such granular flows and gives a deeper macroscopic insight into each of these cases. Thus, our study highlights the efficacy of continuum modeling for predictive purposes, as well as in developing macroscopic conceptual understanding of diverse granular intrusion phenomena.

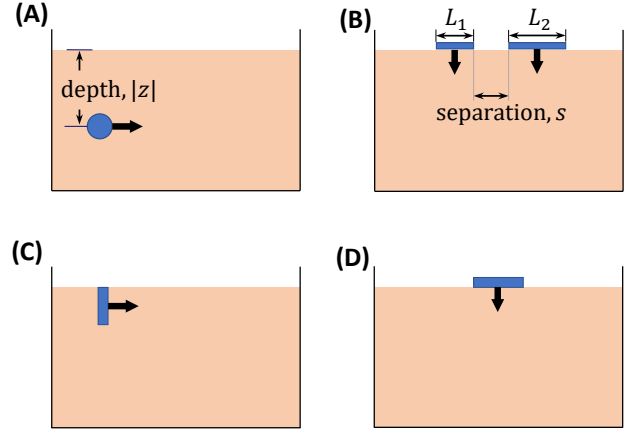


Fig. 1 Schematics of four test cases considered in this study: (A) Horizontal dragging of a submerged cylinder at different depths, (B) multiple-plate vertical granular intrusion, (C) free-surface plowing in under- and over-compacted granular media, and (D) vertical intrusion in under- and over-compacted granular media. Case (A) and (B) will be modeled with the non-dilatant plasticity model (NDPM), and case (C) and (D) will be modeled with the dilatant plasticity model (DPM) to model transient effects.

2 Material and Methodology

We use two constitutive models for representing granular volumes in this study namely: non-dilatant plasticity model (NDPM), and dilatant plasticity model (DPM). We first explain the two models in detail and then explain the numerical method we use for implementing them.

Non-dilatant plasticity model (NDPM): This model is taken from Dunatunga and Kamrin^{27,32}. The model assumes a rate-insensitive, Drucker-Prager yield criterion, incompressible plastic shear flow (with no dilatancy), and cohesionless response in extension whereby the material becomes stress-free below a ‘critical density’. The constitutive flow equations representing the above behavior are shown below. These simultaneous constraints describe the material’s separation behavior, shear yield condition, and tensorial co-directionality, respectively:

$$(\rho - \rho_d)P = 0 \quad \text{and} \quad P \geq 0 \quad \text{and} \quad \rho \leq \rho_d, \quad (1)$$

$$\dot{\gamma}(\tau - \mu_s P) = 0 \quad \text{and} \quad \dot{\gamma} \geq 0 \quad \text{and} \quad \tau \leq \mu_s P, \quad (2)$$

$$D_{ij}/\dot{\gamma} = \sigma'_{ij}/2\tau \quad \text{if} \quad \dot{\gamma} > 0 \quad \text{and} \quad P > 0, \quad (3)$$

for $i, j = 1, 2, 3$.

where,

ρ is the local granular density,

ρ_d is the density of close-packed grains,

μ_s is the internal friction coefficient,
 $P = -\sigma_{ii}/3$ is the local hydrostatic pressure,
 $\dot{\gamma} = \sqrt{2D_{ij}D_{ij}}$ is the equivalent shear rate.
 $\tau = \sqrt{\sigma'_{ij}\sigma'_{ij}/2}$ is the equivalent shear stress,
 $\sigma'_{ij} = \sigma_{ij} + P\delta_{ij}$ is the deviatoric part of Cauchy stress tensor,
 $D_{ij} = (\partial_i v_j + \partial_j v_i)/2$ is the flow rate tensor.

For simplicity, the equations above are expressed in rigid-plastic form, where the flow rate is approximately all due to plastic flow. However, we also include a small elastic component which ensures that below the yield criterion the grains act like a linear-elastic solid. The model evolves the flow by solving the momentum balance equations, $\partial_j \sigma_{ij} + \rho g_i = \rho \dot{v}_i$. We also assume a constant friction coefficient between the granular continuum and solid-body surfaces. We refer to this model as the ‘Non-Dilatant Plasticity Model’ (NDPM). We provide the input material properties used in various cases in the relevant sections. A basic implementation of this continuum modeling approach can be downloaded for Matlab³³.

Dilatant plasticity model (DPM): While NDPM assumes a single critical granular density cutoff for the entire granular volume in the system, this is often not the case in real granular systems. Granular media are known to be able to support stress in a range of densities including close and loose packings⁵. The second model we present addresses this shortcoming of the NDPM model and allows for density evolution in the media⁶. This model takes inspiration from the family of Critical State models^{6,21}. We use a simple rigid-particle version of the Critical State model in which grains are not modeled to crush under hydrostatic loads; rather, they only have a hydrostatic elastic response in this case. When pressure is non-zero, the material is deemed to be in a ‘dense state’ and the density evolution occurs through shearing-based Reynolds dilation/contraction, representing particle rearrangements at the granular level. In a dense state, the packing fraction ϕ is equal to an evolving state variable ϕ_d . Every shearing action in dense media drives the local value of ϕ_d towards a limiting steady-state critical packing fraction, ϕ_c . Furthermore, when the packing fraction varies, the material’s friction coefficient also changes; material with low packing fraction has low consolidation and thus has less strength than more consolidated media.

Thus, in terms of constitutive relations, the simultaneous constraints describing the material’s separation behavior and shear yield condition (eq.1 and eq.2, respectively) remain the same with the two exceptions that the close-packed density, ρ_d , and internal friction value, μ_s , are non-constant local state variables (which vary with time and space), as follow:

$$\rho_d = \rho_g \phi_d, \quad \mu_s = \mu_c + (\phi_d - \phi_c)\chi \quad (4)$$

Here, ρ_g represents the solid grain density, χ represents a dimensionless scaling constant, and μ_c represents the critical-state internal friction value reached by material at steady state (when $\phi_d = \phi_c$). When pressure is positive (the packing is dense), the

evolution of ϕ_d is modeled as:

$$\frac{d\phi_d}{dt} = -3\beta\phi_c\dot{\gamma} \quad (5)$$

where, $\beta = (1/3)(\phi_d - \phi_c)\chi$ is a local dilatancy variable. In the absence of pressure, the material can leave the dense state ($\phi < \phi_d$), but reconsolidates at the current value of ϕ_d unless the material opens up beyond a global lower limit, ϕ_d^{\min} , which defines a minimum density possible for loaded media, below which no connected material states exist. We set this value to 0.45 in all our simulations. Thus, the material maintains can exist in a dense state only for $\phi \geq 0.45$ and the local state variable ϕ_d gets reset to ϕ_d^{\min} (= 0.45) whenever ϕ drops below this value.

In addition to the material’s separation behavior and shear yield condition (eq.1 and eq. 2), the material flow rule has a deviatoric dependence as before (eq.3) but due to dilation now also has a corresponding volumetric component. The volumetric strain-rate is given by the dilatancy variable, β . The plastic flow rate tensor, thus, has the form:

$$D_{ij}/\dot{\gamma} = \sigma'_{ij}/2\tau + \beta\delta_{ij} \quad \text{if } \dot{\gamma} > 0 \quad \text{and} \quad P > 0 \quad (6)$$

Thus, the combination of eqs.1, 2, 4, 5, and 6 collectively represent the Dilatant Plasticity Model (DPM). Note that DPM reduces to NDPM in the limit of $\chi \rightarrow 0$.

The DPM is a more elaborate representation of a granular volume than the NDPM. Thus, many phenomena that cannot be captured accurately by the NDPM are expected to be captured by the DPM. But the NDPM, being a simpler model, is easier to implement and is computationally more efficient to solve. In this study, we aim to highlight the advantages and sufficiency of using each of these constitutive forms on a case by case basis.

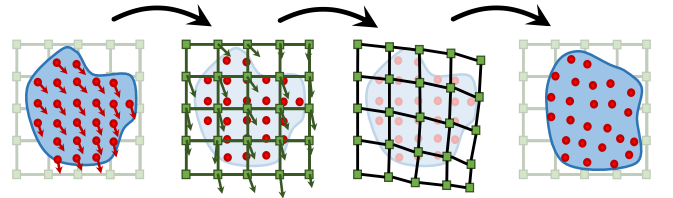


Fig. 2 Sample explicit time integration step in MPM: A sample explicit time-integration step used in an MPM implementation. The Lagrangian tracers called material points (solid red circles) carry the state of material over time and space. The background grid (green squares) assists in integrating the motion on the simulation domain and is reset each step. More details can be found in Dunatunga and Kamrin²⁷.

For the numerical implementation, we use a continuum simulation approach based on the Material Point Method (MPM)³⁴, a derivative of the fluid-implicit-particle (FLIP) method for implementing a continuum description of granular media. The MPM implementation uses a combination of Lagrangian material points, which contain the state of the continuum, and a background computational mesh that is used for solving the equations of motion. Since the state is saved on the material points, the mesh is reset at the beginning of each computational step without any information loss, and thus the method allows for large

deformations in the media without the error associated to large mesh deformations. A schematic representation of an explicit time-integration MPM-step is shown in Figure 2. We use the MPM implementation described in Dunatunga and Kamrin²⁷ to implement the different constitutive equations representing granular volumes assuming 2D plane-strain motion. Thus, the out-of-plane dimension in each simulation is fixed at 1m in this study.

3 Results and Discussion

3.1 Drag and Lift on submerged cylinder dragging

Drag and lift forces on submerged objects in granular media are relevant in processes such as mixing, mining, soil-buried pipelines, and animal locomotion³⁵⁻³⁷. Over the past two decades, several studies³⁸⁻⁴¹ have explored the mechanisms and the variation of these forces by considering the horizontal dragging of submerged, rigid cylinders (at different depths) as a test case. We specifically consider the work of Guillard et al.³⁹, who find that the horizontal drag force on cylindrical objects moving horizontally increases with increasing depth while the vertical lift force plateaus for depths greater than a $O(1)$ factor of the cylindrical diameter. This assumes the starting depth range is deep enough that the cylinders are completely immersed in the granular bed. At low depths near the free surface, the dragging motion of the cylinders results in an accumulation of the media in front of the intruders. This accumulation can augment the depth-dependence of drag forces and thus can change the force trends mentioned above. Thus, we do not consider such a near free-surface depth range in this study and focus on depths $\geq 2.5D$.

The experimental drag and lift results in Guillard et al.³⁹ were obtained by evaluating torques and vertical lifts on horizontal cylinders inside large granular beds being spun about the vertical axis. These drag and lift force responses corresponded to forces encountered during first half rotation of cylinders when the cylinders interact only with fresh material. However, in addition to the reported drag and lift variations, they also observed a reduction in the force response of the media as the cylinders were rotated multiple times and start re-interacting with the disturbed material (after a half rotation of the cylinders along the vertical axis in their rotating cylinder experiments). It is probable that the force reductions in their study happened due to the loosening of the media (from an over-compacted state to a lower packing fraction) as a result of the material loosely reconsolidating in the cylinder wake. As the reported drag and lift relations corresponded to the initial rotations of the cylinder in un-disturbed material, we assume that these force responses can be modeled without a need to consider density variations. Thus we use the NDPM model for numerical studies. A detailed description of the large rotation regime may be tenable using a DPM model, a point we briefly discuss in the conclusions section.

A schematic representation of the cylinder drag case is provided in Figure 1A. For the NDPM implementation, we use a grain density ρ_g of 2520 kg/m³, and a critical packing fraction ϕ_c of 0.60. We calibrate the internal friction coefficient (μ_s) to match the slope of the depth vs drag graph from the experiments and found it to be 0.48. This value seems slightly higher than commonly ac-

cepted value of μ_s (~ 0.4) for glass beads⁴². This minor difference covers the variations in 2D simulations with 3D experiments. The difference also incorporates the variations due to indirect measurements of experimental drag and lift from rotating cylinder experiments³⁹.

The cylinder is modeled as an elastic body with a high elastic modulus, thereby acting as an approximate rigid body. The media-cylinder interface friction coefficient is set to 0.35. The cylinder diameter, D is 4mm, and the in-plane length, L is 1m (as the simulations are 2D plane-strain). We use a $0.20\text{m} \times 0.16\text{m}$ granular bed, and a $5 \times 10^{-4}\text{m}$ spatial resolution (Δx) for simulating these cases.

Figure 3A and B show the comparison of Guillard's experimental data to our continuum results. The linearity of drag vs depth graphs, along with the plateauing of lift vs depth graphs are well captured. The visualizations of plastic strains and strain rates (Figure 3C and D) qualitatively agree with those reported in previous numerical and experimental studies³⁸⁻⁴⁰.

Similar to past DEM studies by Guillard et al.³⁹ and experimental studies by Wu et al.⁴⁰, Figure 3C and D show high localization of granular flows for the depths greater than the lift turnover depth. A further increase in depth after this depth results in minimal/no-change in the material flow profile and adds only to the local lithostatic pressure head. The drag and lift forces are also differently-related to this flow localization. While the drag forces continue to increase linearly with depths beyond this depth, the lift forces become saturated around this depth indicating a possible correlation between the flow and forces. A deeper analysis of the variation and the mechanics of the force distributions on different faces of the intruders in such scenarios is required in future studies.

Thus, the case of dragging submerged cylinders provides an example where even a simple model like NDPM is able to capture the observed intrusion behavior.

3.2 Vertical drag in two-plate granular intrusions

Multi-body intrusions offer another commonly encountered scenario in various real-life situations. Several researchers in the past⁴³⁻⁴⁵ have examined the dynamics of granular intrusions involving multiple intruding bodies. The case we study specifically takes inspiration from the work of Swapnil et al.⁴⁵ who examined the variation of vertical drag forces on a pair of parallel rigid plates during vertical intrusions as a function of the separation between them. They observed a peak in the average vertical drag as the separation between the plates was increased. We use NDPM for investigating this case to capture and obtain a macroscopic insight into the phenomenon. We also conduct experiments to verify claims that follow from theoretical analysis of the NDPM model.

A schematic representation of the case is given in Figure 1B. This case aims to understand the capability of continuum modeling in capturing the macroscopic phenomenon along with understanding the underlying mechanics. We use a set of generic NDPM fitting properties from the earlier case, i.e. a grain density, ρ_g of 2520 kg/m³, a critical packing fraction ϕ_c of 0.6, but a

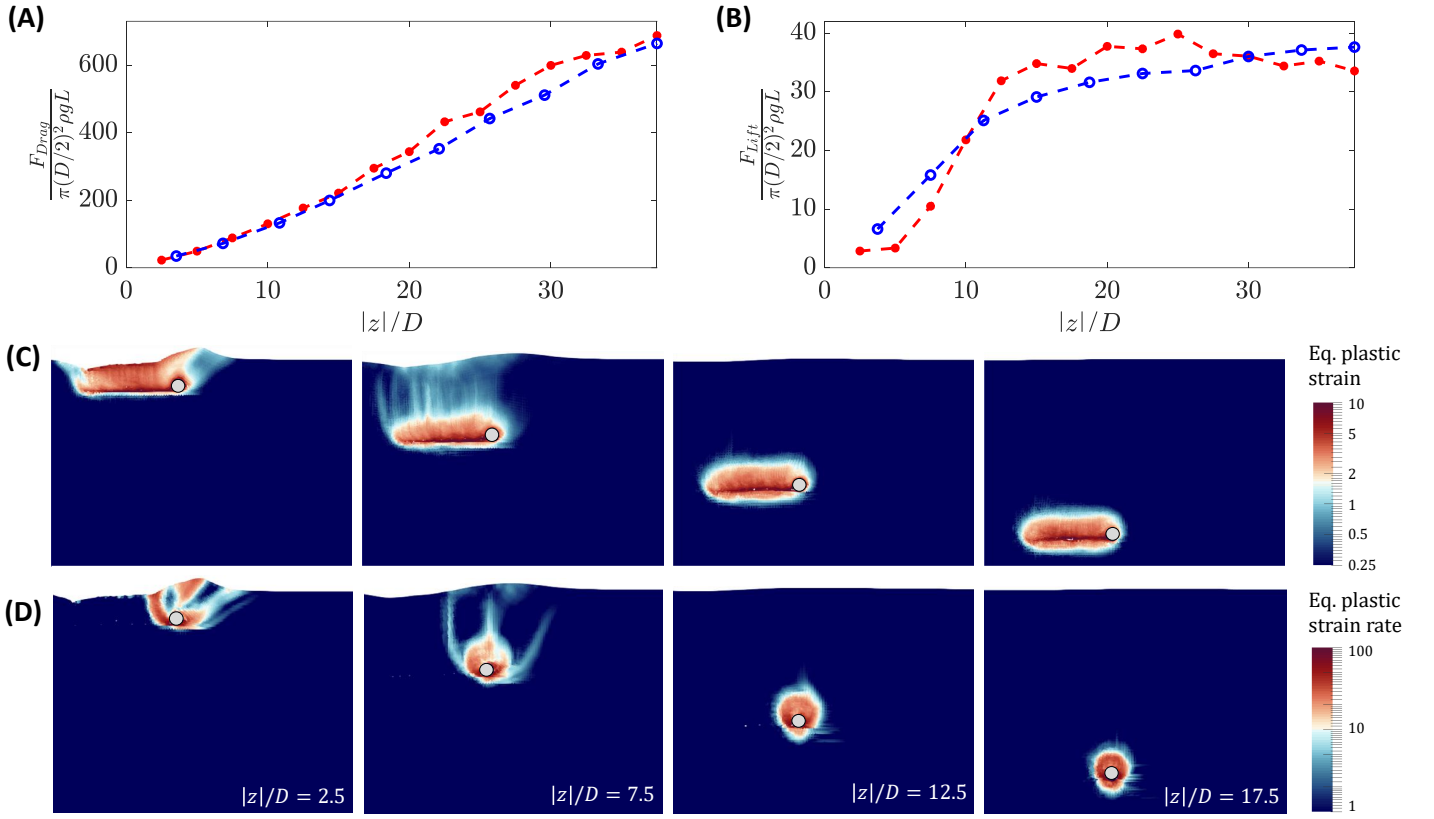


Fig. 3 Case 1: Experimental vs Simulations results for drag and lift on submerged cylinders: Comparison of experimental data³⁹ (in blue) and the continuum simulations results (in red) for variation of (A) drag, and (B) lift on submerged cylinder motion in granular media with depth, $|z|$. The drag and lift forces are non-dimensionalized with characteristic force $\pi(D/2)^2 \rho g L$ where D is the cylinder diameter, ρ is the effective medium density, g is the gravity, and L is in-plane cylinder width. Both experiments and continuum results use $D = 4\text{mm}$, $\rho = \phi_c \rho_{grain} = 1512\text{kg/m}^3$, and $g = 9.8\text{m/s}^2$. The value of L was 1m for continuum simulations. Similarly depth is non-dimensionalized with cylinder diameter, D . Variation of macroscopic state variables (C) equivalent plastic strain, and (D) equivalent plastic strain rate at four different depths [10, 30, 50, 70] mm. The gray circle indicates the cylinder position and the drag direction is from left to right. See Movie S1 for visualizing material flow over time for cylinder drag cases considered in (C) and (D).

more common internal friction coefficient μ_s of 0.4 for the glass beads⁴². The plates were modeled as stiff elastic bodies with vertical displacement of control points assigned; thus, the plates act as quasi-rigid objects with a common fixed downward velocity. The intrusion velocity was set to 0.1m/s in all simulations, and the media-plate surface friction was set to 0.35. We use a $1.2\text{m} \times 0.6\text{m}$ granular bed, and a $1.25 \times 10^{-3}\text{m}$ spatial resolution (Δx) for simulating these cases.

Understanding single plate intrusions

We begin by first analyzing the variations of vertical drag forces in single plate intrusions. Figure 4A shows the drag forces on vertical plate intrusions under NDPM for various plate widths at a constant intrusion velocity of 0.1m/s . Before analysing the simulation results, we perform a scaling analysis of the problem assuming the NDPM equations hold, in order to predict the dependence of drag on various system parameters. In this case, we expect the drag force, on a vertical intruder of width L and in-plane width w at a depth of z , to depend on various system parameters, i.e. intruder dimensions (w and L), depth z , close-packed media density ρ_d , gravity g , the media's internal friction μ_s , the media-intruder interface friction μ_f , and the velocity of intrusion v . Using scaling

analysis, with base units of length as L , time as $\sqrt{L/g}$, and mass as ρL^3 , we obtain:

$$F^D = \rho_d L^3 L (\sqrt{L/g})^{-2} \hat{f}(\mu_s, \mu_f, z/L, w/L, v/\sqrt{gL})$$

$$= \rho_d g L^3 \hat{f}(\mu_s, \mu_f, z/L, w/L, v/\sqrt{gL}) \quad (7)$$

The dependence of F^D on z can be divided into two regimes. (1) At low depths $z \ll L$, the variable z/L is negligible and can be ignored. And (2), at larger depths, the drag forces F^D are known to show a linear dependence on depth (after an initial jump in the vertical drag near free surfaces^{46–49}). In both of these regimes, we can set the dependence of F^D on w to be linear assuming the plane-strain nature of the intrusions. We can also consider F^D to be independent of velocity v (low-velocity regimes) based on the work of Swapnil et al.⁴⁵ (and our simulation verifications).

With the above assumptions, in the $z \ll L$ regime, we obtain:

$$F^D = \rho g L^3 (w/L) \hat{f}(\mu, \mu_f)$$

$$\rightarrow F^D/w = \rho g L^2 \hat{f}(\mu, \mu_f)$$

$$\rightarrow F \propto L^2. \quad (8)$$

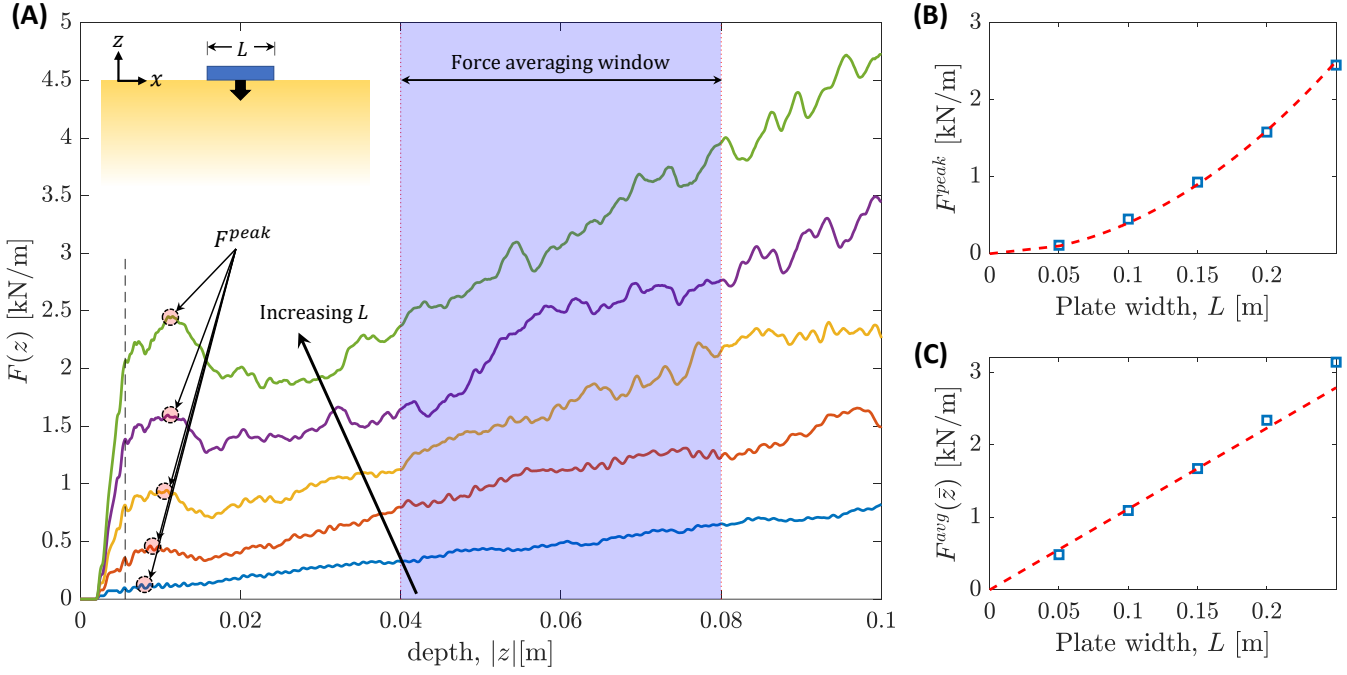


Fig. 4 Case 2: Vertical intrusion of single plates. (A) Variation of drag forces with intrusion depth for plates of various widths, L (0.05, 0.10, 0.15, 0.20, 0.25 m) during single-plate vertical granular intrusion. The arrow shows the direction of increasing L . The simulations are plane-strain and glass bead properties are used for simulating granular media ($\rho_g=2520 \text{ kg/m}^3$, $\rho_c = 0.6$, $\mu = 0.4$). Each data series on the left graph was time-averaged over a 0.5ms window to remove high-frequency force fluctuations. The vertical black dotted line in (A) shows the depths after which this averaging window includes sufficient data. Dependence of (B) initial force peaks, and (C) average drag forces on plate widths in single plate intrusions (blue squares). The corresponding quadratic and linear fits for (B) and (C) are shown as red dotted lines in corresponding graphs. The force peaks are shown with arrows in the left graph, and the time window used for calculating the average forces is the highlighted blue region (force averaging window) on the left graph.

And in the latter, moderate-depth regimes with $F^D \propto z$, we obtain:

$$\begin{aligned}
 F^D &= \rho g L^3 (w/L) (z/L) \hat{f}(\mu, \mu_f) \\
 \rightarrow F^D/w &= \rho g z L \hat{f}(\mu, \mu_f) \\
 \rightarrow F &\propto zL.
 \end{aligned} \tag{9}$$

Thus, from the scaling analysis, we expect the drag forces per unit in-plane width F ($= F^D/w$) (unit N/m) to have a quadratic dependence on plate width, L , near the free surface, and a linear dependence on plate width at larger depths.

Using the simulation's force output, in Figure 4B and C we plot the observed relationships between F and L at, respectively, a small depth (where initial peaks occur) and in a deeper regime, where linear force variations are predicted. For data clarity, the forces in Figure 4C are averaged over a depth window, i.e. $F^{avg} = (\int_{z_i}^{z_f} F(z) dz) / (z_f - z_i)$. The expected trends from the dimensional analysis are apparent. Besides our own simulation results, the linear dependence of drag force on intruder area, once deep enough, is a well studied relation^{46–48}. We reiterate that our simulations are all in the quasistatic regime. Thus, the velocity contributions are negligible in comparison to static force contributions in our study.

Physically, the initial force maxima (F^{peak}) in the force vs. displacement graphs of Fig. 4A correspond to the force requirements

for initiating media flow in the system. The F^{peak} force contributions enable the beginning of flow by initiating the shearing of the media, which exists at some finite strength due to finite pressure under the plate. From slip-line theory for granular intrusions⁵⁰, the flow develops a wedge-shaped no-shear-zone below the intruder, which has an acute angle of $\pi/2 - \tan^{-1}(\mu)$ (where μ represents the material internal friction). Thus, the requirement of shearing media of a finite strength along the wedge shaped shear zone is responsible for these force contributions. We can obtain an intuition for the initial L^2 dependence of force by considering the conventional limit analysis for indentation of materials with yield stress Y , common in manufacturing processes such as drawing and blanking⁵¹. In such cases, indenter force per unit out-of-plane width, F , varies as $F \propto Y \times L$ for L the indenter plate length. In frictional media, the strength is pressure sensitive. With $Y = \mu \times P$ and supposing P grows linearly along the edge of the no-shear-zone wedge, the mean strength along the edge grows $\propto L$. Substitution of $Y \propto L$ in the limit analysis formula then gives the observed quadratic dependence of the drag force on L . We do not further investigate these forces but identify that the existence of small regions of under-compacted granular media near free surfaces is expected to suppress the growth of such forces in many cases (see figure 8D). Our simulations indicate that the drag forces' dependence of F on L enter linear regimes at depths $z \sim O(10^{-1})L$. These forces are unique from the 'added

mass' effects⁵² and other macro-inertial effects^{46,47} in granular impacts that are common in high-speed intrusion (and vary $\propto v^2$) since our intrusion velocities are small.

Two plate intrusions

The above scaling analysis gives an important insight into the case of multibody intrusions. In the purview of eq. 9, we expect that two plates intruding far away from each other and at a moderate depth, will experience the same net vertical drag as that experienced by a single plate with an equivalent surface area — the linearity in L (eq.9) indicates that this equality should hold for any ratio of areas between the two plates. Thus, any combination of plate widths should experience the same forces both when they are infinitely far apart and when they have no separation. This analysis does not provide any information on the force variations when the plates are close but are at a finite distance from each other. However, physical intuition suggests that the presence of plates in the vicinity of each other will restrict the material flow, which should increase the drag on each plate. Given that the plates experience equal net forces at infinite and zero separation between them, we expect the force response to have a critical point at a finite value of separation (unless the force response is constant). The work of Swapnil et al.⁴⁵ explored this variation and found a peak in forces at a unique separation between the plates. Note that near the free surface ($z \ll L$), we do expect drag forces at zero separation to be higher than at infinite separation due to the quadratic dependence of forces in this regime — the ratio of forces for plate lengths of L_1 and L_2 would be $F_0/F_\infty = (L_1 + L_2)^2 / (L_1^2 + L_2^2)$ which is always greater than 1.

Figure 5A and B show the variation of force for different combinations of plate widths and plate separations. Continuum modeling shows the existence of force peaks for both equal plate cases (Figure 5A) and unequal plates cases (Figure 5B). Our observations are in accord with similar experiments by Swapnil et al's⁴⁵ for equal plates. As the continuum modeling successfully captures the behavior, the detailed material states in these simulations can now be used to identify the macro-mechanical origins of the phenomena. We visualize the material flow by plotting snapshots of the plastic strain in a few of these cases. The plastic strain fields before, at, and after the force peak in Figure 5C and D, suggest a macro-mechanical picture. We observe higher granular flow interaction between the two plates as the separation between the plates is decreased. For a single plate intruder, any neighboring flow restriction is expected to make it more difficult to push the material during the intrusion. Thus, decreasing plate separation results in increasing drag on each plate. Once the plates are sufficiently close, a large wedge-shaped rigid zone forms spanning the plates, causing the two plates to act as a large single plate. Thus, any further reduction in the separation does not result in additional flow restriction. Instead, it leads to a reduction in the effective area of the merged plate systems, and thereby the drag forces decrease upon a further decrease in separation. It is interesting to note that the material flow profiles when the two plates are together or far-separated are similar to the classical plasticity solution of Prandtl⁵³ for yielding of metals upon indentation under a plate, characterized by a single rigid wedge of media

under the indenter and flow emanating from both edges of the wedge. However, when the plates are separated but very close, the flow profile looks similar to the indentation plasticity solution of Hill⁵⁴, characterized by two smaller wedges under the plate and flow emanating only from the two outermost edges.

To understand the behavior of the flow solutions, we re-derive the scaling relations for combinations of plates of different lengths L_1 and L_2 ($L_1 \leq L_2$) assuming NDPM, similar to the single plate case. Using base units of length as $L_{avg} = 0.5(L_1 + L_2)$, time as $\sqrt{L_{avg}/g}$, and mass as ρL_{avg}^3 , we get:

$$F^D = \rho_d g L_{avg}^3 \hat{f}(\mu_s, \mu_f, z/L_{avg}, s/L_{avg}, w/L_{avg}, L_1/L_2, v/\sqrt{gL_{avg}}).$$

With similar assumptions as before in the moderate-depth regime ($F \propto z$),

$$F^D = \rho_d g z L_{avg} w \hat{f}(\mu_s, \mu_f, s/L_{avg}, L_1/L_2).$$

Defining a non-dimensional force, $\tilde{F} = F^D / \rho_d g z L_{avg} w$, we get

$$\tilde{F} = \hat{f}(\mu_s, \mu_f, s/L_{avg}, L_1/L_2) \quad (10)$$

and for equal plates, $L_1 = L_2$, $L_{avg} = L$ and we get:

$$\tilde{F} = \hat{f}(\mu_s, \mu_f, s/L). \quad (11)$$

Therefore, if the NDPM model suffices in describing the physics of two-plate intrusion, we expect the above relation to describe a master curve that collapses data for plates of various L intruding into the same media.

Based on eq.10, for $F \propto z$, we obtain following relations for peak separation (s_p) and corresponding peak force (F_p) values:

$$s_p = L_{avg} \hat{f}_1(L_1/L_2, \mu_s, \mu_f), \text{ and} \quad (12)$$

$$F_p = \rho_d g z L_{avg} \hat{f}_2(L_1/L_2, \mu_s, \mu_f). \quad (13)$$

For equal plates ($L_1 = L_2 = L = L_{avg}$) we get

$$s_p = L \hat{f}_1(\mu_s, \mu_f), \text{ and} \quad (14)$$

$$F_p = \rho_d g z w L \hat{f}_2(\mu_s, \mu_f). \quad (15)$$

Note that F_p has units of force per out-of-plane length. Also note that, under these relations, the only material properties that influence the peak force and separation are the friction coefficient(s) and density; the sole length scale comes from the plate itself. This makes sense when the smallest in-plane feature ($\min(w, L, s)$) is larger than a $O(1)$ factor of the grain diameter. However, the exact value of $O(1)$ needs to be calculated experimentally. Swapnil et al.⁴⁵ explored the dependence of force-peak separation s_p/d with intruder size, L/d , when the intruder size is close to the grain diameter, d (L/d range 1–6). Interestingly, their data appears to agree with our proposed linear dependence $s_p \propto L$ at intruder sizes as low as 3-4 grain diameters.

We also verify these drag force variations and the peak separation scaling relation with vertical intrusion experiments and compare them to calibrated continuum simulations (see figure 6 for the details). A DENSO VS087 robot arm intruded an appara-

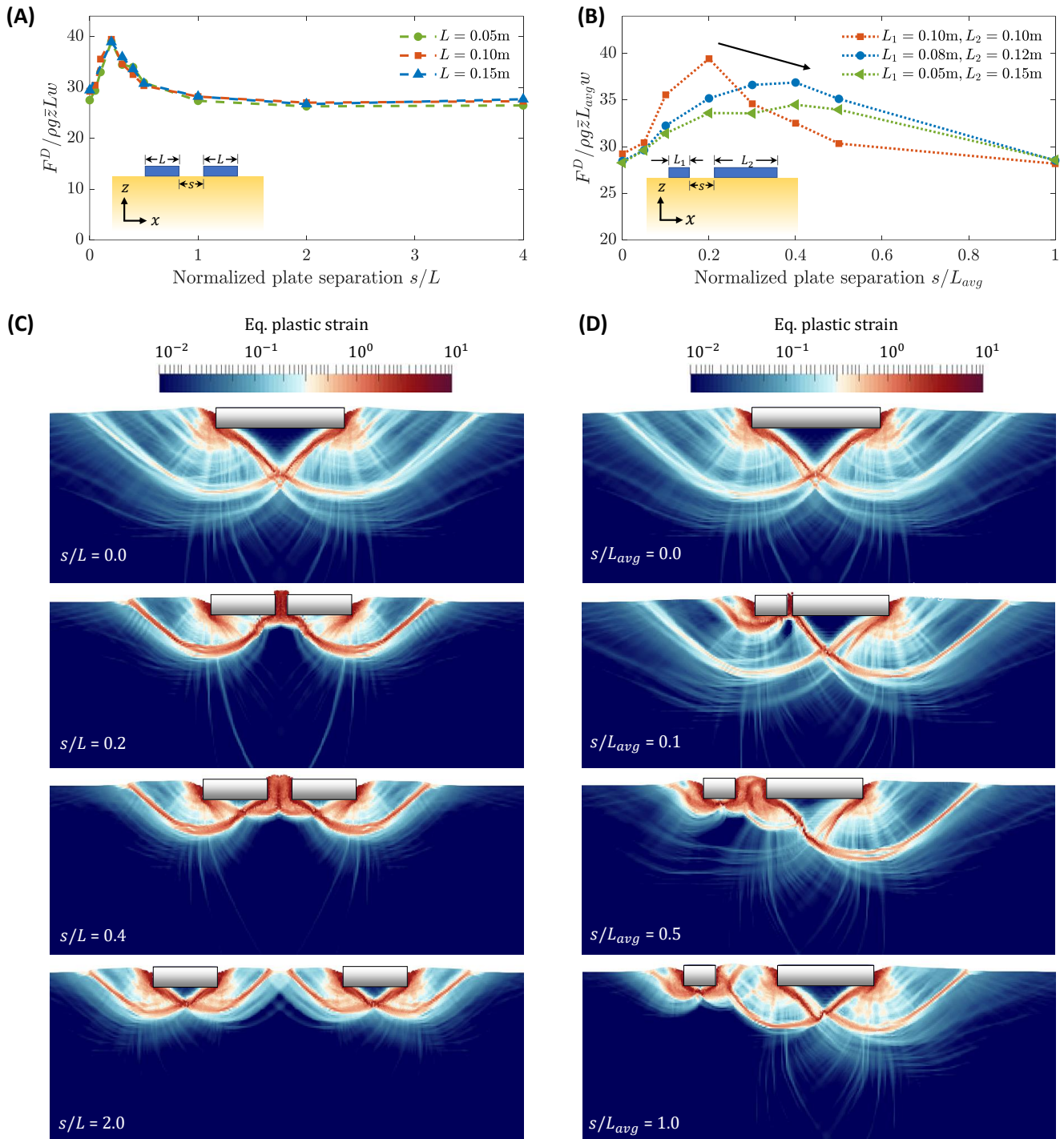


Fig. 5 Case 2: Vertical intrusion of two parallel plates. (A) Variation of vertical drag (normalized) with plate separation, s (normalised to plate width L) for equally sized plates. (B) Variation of vertical drag with plate separation, s (normalised with average plate width $L_{avg} = (L_1 + L_2)/2$) for unequally sized plates. Flow fields visualization using equivalent plastic strain for (C) equally sized ($L = 0.10\text{m}$ each), and (D) unequally sized ($L_1 = 0.05\text{m}$ and $L_2 = 0.15\text{m}$, bottom) plates. The forces F^D are averaged over a depth range of $0.04 - 0.08\text{m}$ for all the cases and an average depth, $\bar{z} = 0.06\text{m}$, $w = 1\text{m}$, $g = 9.8\text{m/s}^2$, $\rho = 1512\text{kg/m}^3 (= \rho_g * \phi_c)$ is used for scaling vertical-axis in (A) and (B). The simulations are plane-strain and glass bead properties are used for simulating granular media ($\rho_g = 2520\text{ kg/m}^3$, $\rho_c = 0.6$, $\mu = 0.4$). See Movie S2 for visualizing material flow over time for the two cases considered in (C) and (D).

tus that held pairs of steel plates at various separations into a bed of loosely consolidated Quikrete Pool Filter Sand with grain density $\rho_g = 2520\text{kg/m}^3$, and effective close-packed density $\rho_d = 1512\text{ kg/m}^3$. The internal friction value of this medium was $\mu_s = 0.72$

based on angle of repose measurements from experimental tilting tests, with the media globally fluidized for 15 seconds to a loose initial packing fraction of $\phi \approx 0.58$ for all trials. All intrusions were performed at 11mm/s , where speed dependence of the force re-

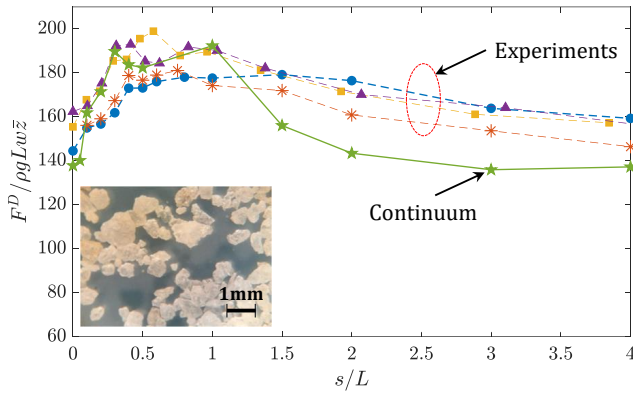


Fig. 6 Case 2: Experimental verification of peak force phenomenon in two-plate intrusions: The comparison of experimental data (dotted lines) and calibrated continuum simulations (solid line) for two (equal) plate intrusion experiments. The experiments use plates of width (L) 15mm (blue data with \bullet marker), 20mm (orange data with $*$ marker), 26mm (yellow data with \blacksquare marker), 29mm (violet data with \blacktriangle marker), and the continuum model uses a plate of width 10mm (green data with $*$ marker). Quikrete Pool Filter Sand with grain density $\rho_g = 2520 \text{ kg/m}^3$ was used (inset shows microscopic view). The effective critical density ρ_c and angle of repose of the sand was found to be 1512 kg/m^3 and $36^\circ \pm 1$ resp. All of the paired plates have a 1 : 5 horizontal aspect ratio. The continuum results correspond to plane-strain two plate intrusions with drag forces F^D averaged over a depth range of 0.06 – 0.08m for all the cases and an average depth, $\bar{z} = 0.07 \text{ m}$, $w = 1 \text{ m}$, $g = 9.8 \text{ m/s}^2$, $\rho = 1512 \text{ kg/m}^3 (= \rho_g * \phi_c)$ is used for scaling the vertical axis. The material properties are calibrated based on experimental data with $\rho_g = 2520 \text{ kg/m}^3$, $\rho_c = 0.6$, $\mu = 0.72$ ($= \tan^{-1} \theta_{repose}$).

response is negligible. Over 128 trials, the net resistive forces on the pair of intruding plates were measured using an ATI Mini40 force transducer. We observed a satisfactory match between the experiments and the simulations. The fact that the experimental data for different values of L collapse onto a single dimensionless master curve supports the robustness of the scaling relation implied by NDPM in eq 11.

We also briefly explore, in our simulations, the effect of changing plate width ratios on the peak separation distance (s_p), and the peak separation force (F_p) in our study (see figure 5B). We find that F_p monotonically decreases from a maximum value to F_∞ as the plate ratio decreases from 1 to 0 (note that plate-ratio L_1/L_2 is always ≤ 1 as $L_1 \leq L_2$ by definition). The normalized peak separation distance (s_p/L_{avg}) increases with decreasing plate-ratios (L_1/L_2). The peak separation relations are also expected to be a function of μ_s from scaling analysis (eq. 13). Thus, an in-depth shape and material property dependence characterisation of this phenomenon is relegated to future study.

There is an interesting connection between the drag increase in multi-plate granular intrusion and swimming in water. Minetti et al.⁵⁵ reported that during swimming, an optimal finger spacing (12°) increases the thrust on hands by 8.8% compared to closed fingers. Thus, during the propulsive stroke in swimming humans, a slight separation between fingers increases propulsive thrust, similar to our observation of increasing intrusion force as granular intruders separate slightly^{55,56}. Since both the fluid and gran-

ular cases appear to have a rationale at the continuum scale, it suggests there could be additional phenomena that transfer between the two media at the appropriate length scales. However, any analytical comparison would have to reconcile the notably different constitutive relations.

3.3 Drag variations in the plowing of granular media

This case takes inspiration from the work of Gravish et al.⁵⁷ who studied drag force fluctuations in the plowing of granular beds at different initial packing fractions. A Discrete Element Method (DEM) based study of the case was also performed by Kobayakawa et al.⁵⁸. Both of these studies observed increasing drag forces fluctuations with an increasing initial density of the granular beds. Similar force fluctuations were observed by Kashizadeh and Hambleton⁵⁹ on reduced order modelling of the ploughing processes in sands and by Jin et al.⁶⁰ in development of a new single-gravity (1-g) small scale testing methodology. As this phenomenon directly relates to the changing density of the media, we use the more detailed DPM model for this case.

A schematic representation of this case is given in Figure 1C. Both of the reported studies were performed in 3D while our simulations are 2D plane-strain. Characterising the effects of this difference in our studies is difficult, so we do not attempt an exact match. Nevertheless, we do expect the 2D simulations to capture the phenomenon qualitatively and the drag forces to be similar in their magnitudes. We once again use the glass bead material properties used in the previous case. We use a grain density ρ_g of 2520 kg/m^3 , a critical packing fraction ϕ_c of 0.60, a steady-state critical internal friction μ_c of 0.4, and a scaling coefficient χ of 2.5. Similar to previous cases, the plates are modeled as elastic bodies with high elastic modulus to act as rigid bodies. The media/plate interface friction was set to 0.35. We use a $2.4 \text{ m} \times 0.4 \text{ m}$ granular bed, and a $4 \times 10^{-3} \text{ m}$ spatial resolution (Δx) for simulating these cases. The plowing plate dimensions are $0.03 \times 0.08 \text{ m}^2$.

Figure 7 shows the variation of horizontal drag forces from the Gravish et al.⁵⁷ experiments alongside our continuum simulations. The continuum results are scaled proportionally to the out-of-plane width in Gravish et al.⁵⁷. The mean drag force and force fluctuations from continuum modeling are plotted in Figure 7D and E, showing smooth forces transition to larger, fluctuating forces as the initial packing fraction rises above ϕ_c . The same trends can be seen in experiments, c.f. Figure 7A and B. A visual free surface comparison between experiments and the simulations also shows the similarity of flows as ϕ_i varies, c.f. Figure 7C and F.

The observed shear patterns, free-surface profiles, and force fluctuations shown in Figure 7A-C are in accord with the shear-softening (shear-strengthening) of over-compacted (under-compacted) granular media that is built-in to the DPM model. In a sample initially under-compacted ($\phi_i < \phi_c$), shear deformations cause compaction, resulting in higher densities along the sheared regions than in the bulk (see eq.5). This density increase results in higher shear strength along the shear zone (see eq.4). Thus, further loading in such systems induces shear to occur in the weaker material adjacent to the shear band, which effectively

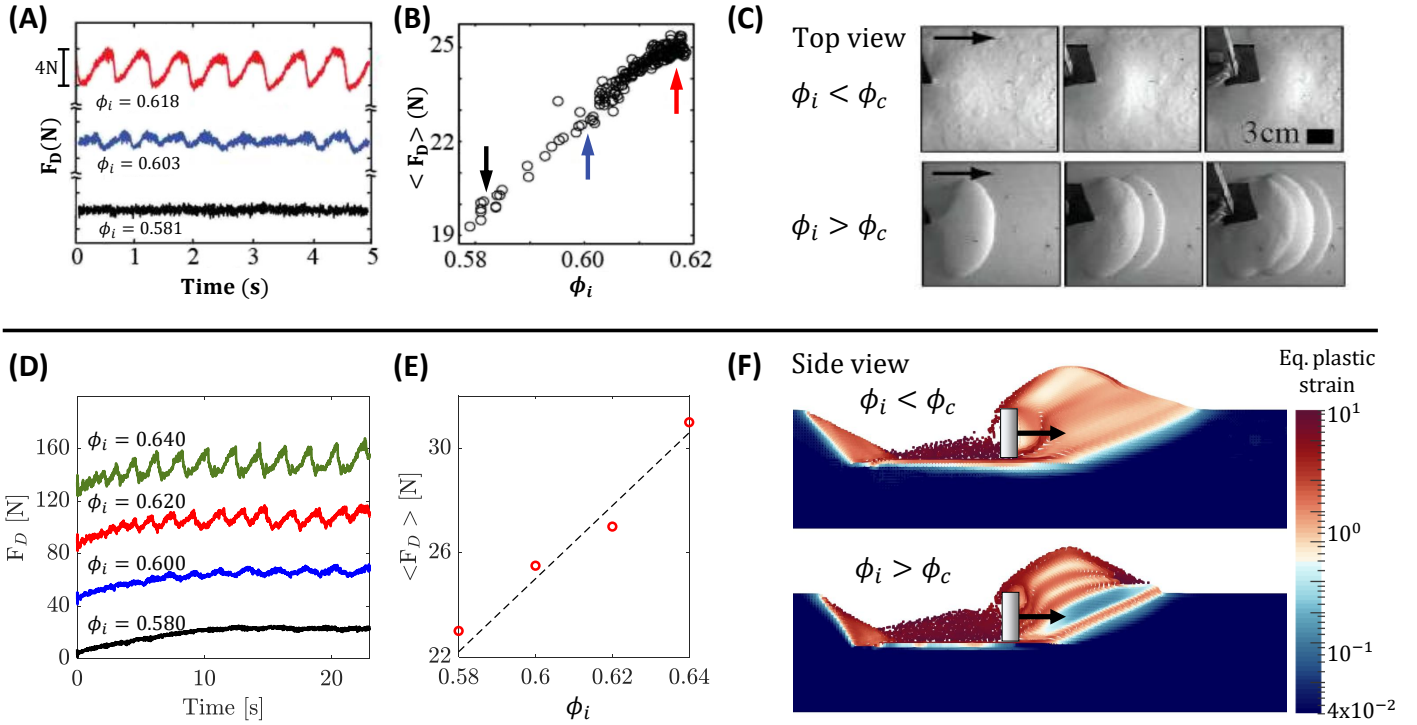


Fig. 7 Case 3: Force fluctuations during plowing. Variation of drag forces at various initial packing fractions in Gravish et al's⁵⁷ experiments: (A) time variation of drag forces, and (B) average drag forces. The average values of forces for three initial packing fractions in (A) are shown with corresponding colored arrows in (B). Corresponding continuum simulations: (D) Time variation of drag forces (force plots for consecutive ϕ_i are shifted vertically by 0, 40, 80, and 120N respectively for improved visualization), and (E) averaged drag forces. Visualisation of the free surface in under/over compacted granular media: top view from Gravish et al's⁵⁷ experiments (C), and side view in continuum simulations (F). The simulations are plane-strain and glass bead properties are used for simulating granular media ($\rho_g=2520 \text{ kg/m}^3$, $\phi_c = 0.6$, $\mu = 0.4$, $\chi = 5.0$, $\phi_{min} = 0.45$). See Movie S3 for visualizing time evolution of material front during plowing of under- and over-compacted media from experiments and simulations. Figure (A), (B) and (C) are modified from Gravish et al⁵⁷. [Photo credits: (C) N. Gravish, P. B. Umbanhowar and D. I. Goldman, Georgia Institute of Technology]

spreads the shearing in such systems. On the other hand, in the over-compacted case, shear deformations dilate the material, resulting in lower density in the sheared region than in the bulk, which results in lower shear strength there. Hence, continued loading causes shear to accumulate along the thin zone of initial failure causing the appearance of a strong shear band. This process continues until the total force requirement for shearing along the existing band exceeds that for creating a new shear band in the bulk (after which the same process repeats itself). Thus, in over-compacted media, a visually separable shear band formation pattern occurs (Figure 7F). In initially over-compacted cases ($\phi_i > \phi_c$), increasing the initial packing fraction of the media results in an increased plate motion requirement between successive shear band formations (due to increased strength of the media in the bulk) and thus the force fluctuation magnitudes increase (and their spatial frequency decreases) with increasing packing fraction (observed also by Gravish et al.⁵⁷).

3.4 Development of a shear deformation zone in plate intrusions

This last case takes inspiration from the work of Aguilar and Goldman⁵² and highlights the capability of the basic DPM model in capturing the *development* of the flow profile during vertical in-

trusion of single plates. A schematic representation of the case is given in Figure 1D. Aguilar and Goldman⁵² postulated that the formation of a rigid No Shear Zone (NSZ) ahead of a flat plate during vertical intrusion is an incremental growth process. In three dimensions, this growth takes the form of a rigid frustum shape which grows from a low height frustum with a fixed base (matching the shape of the intruder) to a fully developed cone/pyramid at the completion of the mechanism. For a circular base, the final shape is a cone. In two-dimensions, like our case, this would translate to successive isosceles trapeziums (with larger parallel edges matching the intruder's intruding edge) leading to a wedge shape with the base as the intruder's leading edge.

Figure 8 shows the variation of intrusion forces and successive velocity profiles in undercompacted granular intrusion experiments compared to our continuum simulations. We model the granular media, poppy seeds, with the DPM to incorporate the effect of density transitions. We use material properties for poppy seeds with a grain density $\rho_g=1100 \text{ kg/m}^3$, a critical packing fraction $\phi_c=0.60$, a steady-state critical internal friction $\mu_c=0.53$, and a scaling coefficient $\chi=5.0$. We use a $0.5\text{m} \times 0.2\text{m}$ granular bed, and a $5 \times 10^{-4}\text{m}$ spatial resolution (Δx) for simulating these cases. The intruding plate dimensions are $0.04\text{m} \times 0.02\text{m}$.

The force trends from simulation qualitatively match the experimental trends from Aguilar's experiments (compare Figure 8A to

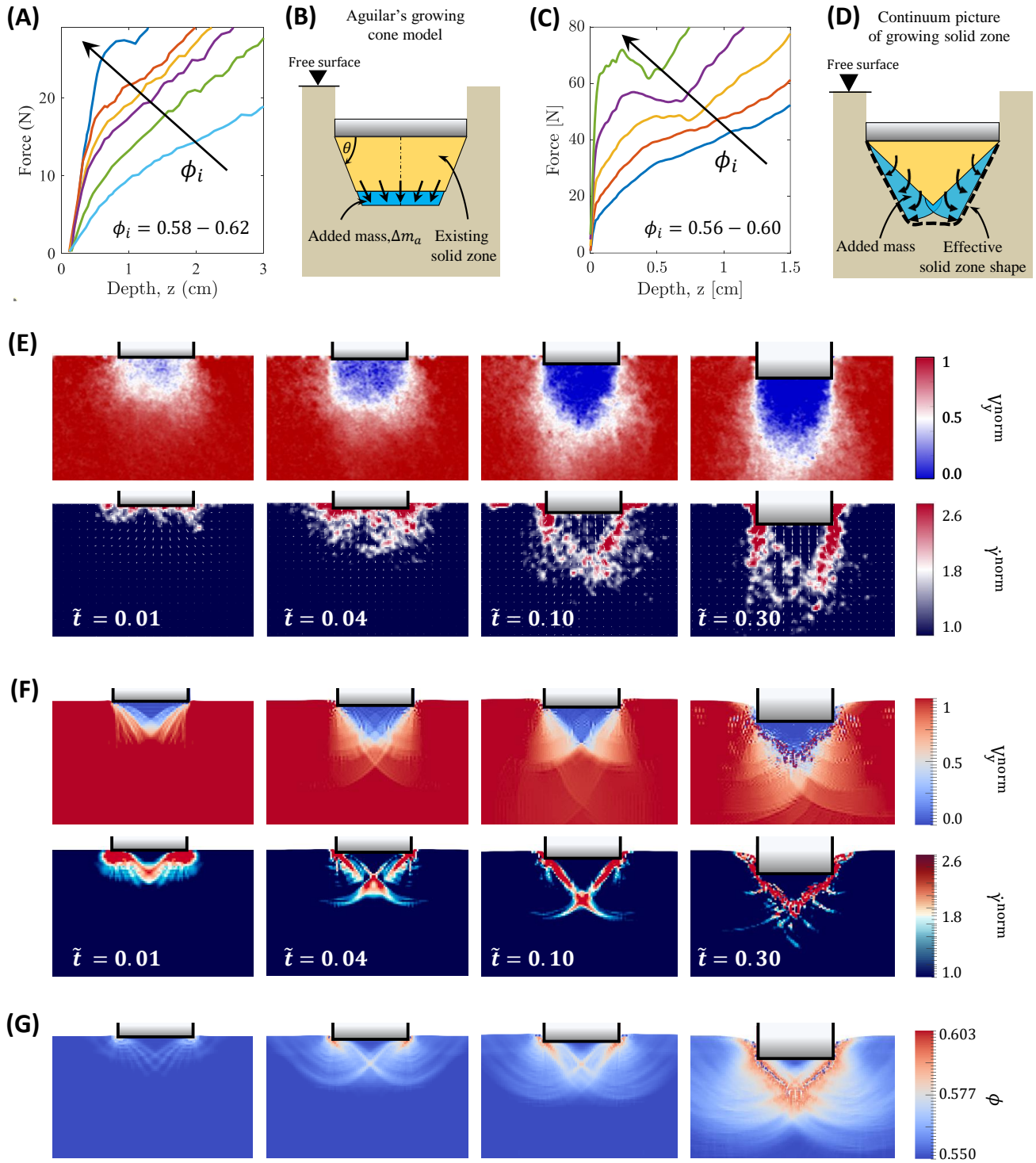


Fig. 8 Case 4: Material front development during vertical intrusion: (A) Experimental data from Aguilar and Goldman⁵². The experiments intruded a circular plate of 0.051m diameter into poppy seeds ($\rho_g = 1100 \text{ kg/m}^3$) at various initial packing fractions (ϕ_i). (B) Schematic of Aguilar and Goldman's cone growth model⁵². (C) MPM simulation results: Force data from 2D plane strain simulations. We intrude 0.04m wide flat plates into material with properties $\rho_g = 1100 \text{ kg/m}^3$, $\mu_c = 0.53$, $\phi_c = 0.60$, and $\chi = 5.0$, as calibrated to poppy seeds. (D) Mechanism of solid zone development apparent from continuum modeling. (E) PIV analysis of constant speed plate intrusions. Experiments conducted by intruding $L = 40 \text{ mm}$ wide rectangular flat plates next to a clear plexiglass wall at a constant low speed, $v = 150 \text{ mm/s}$, in loosely packed poppy seeds. The initial three frames represent the cone growth phase and the last frame ($\tilde{t} \sim 0.30$) shows the stability of the cone at later stages of the intrusion. Time is non-dimensionalized ($\tilde{t} = t/t_0$) by $t_0 \equiv L/v$. The velocity is normalized by intrusion speed, v , and strain rates by $\dot{\gamma}_0 \equiv 1/t_0$. We plot these results in the intruder's frame of reference. (F) MPM simulation results: Vertical velocity and equivalent plastic strain rate fields during vertical intrusion in initially under-compacted media ($\phi_i = 0.55$) for material properties discussed in (C). We also show the evolution of packing fraction from continuum modeling in (G). See Movie S4 for visualizing material flow over time for various initial packing fractions (ϕ_i) including the one considered in (F).

8C), keeping in mind that Aguilar uses a 3D circular plate while our simulations are in 2D plane-strain. In a set of separate experiments using a rectangular plate intruder and PIV (Figure 8E) we observed the flow zone development appears similar to continuum results (Figure 8F). These trends also agree with general observations from a 3D DEM study done by Feng et al.⁶¹. The Aguilar and Goldman⁵² study presents a model whereby the rigid cone emerges from a growing rigid frustum of constant base angle that gets progressively longer until converging to the final cone shape (Figure 8B). However, in our simulations, the zone actually starts as a ‘short’ wedge coincident with the plate bottom, having a large obtuse apex angle (expected by slip-line theory to be approximately $\pi/2 + \tan^{-1} \mu_i$ for μ_i the friction at the initial density) due to the low initial packing fraction of the media. The rigid front then grows by ‘fanning out’ from the diagonal edges (see Figure 8D), as the edges represent the zone experiencing maximum shear-compaction and hence the most strengthening. This growth can be observed as well from density variations, shown in Figure 8G. The growing density of the region results in an increasing but variable internal friction value in the zone below the intruder, and results in the development of a progressively sharpening, quasi-rigid trapezoid-like shape under the plate. As the intruder moves deeper, the process converges to a final wedge shape (with a sharper half angle equal to ‘ $\pi/2 - \tan^{-1} \mu_c$ ’). Thus the DPM model provides an apt description of the observed behavior in undercompacted granular intrusion.

4 Conclusions

The four cases we study show that relatively simple, friction-based plasticity models capture a large variety of granular intrusion phenomena. Moreover, they provide a useful macroscopic understanding of granular intrusion processes, which are often primary interests in engineering applications, and remove the additional complexity of trying to parse the physics from the grain scale. The simplicity of these continuum models also streamlines this understanding, both by exclusion – i.e. if such a model works, it implies that mechanisms or effects lying outside the model’s formulation are not crucial to the outcome – and by opening up useful scaling analyses as we have utilized throughout. Such simplifications will certainly limit the accuracy of these models in a variety of cases, but an incremental approach of adding physical augmentations (such as micro-inertial effects, particle size effects, or evolving fabric variables) provides a systematic approach for exploring the underlying physics in diverse cases. For instance, we do not use $\mu(I)$ rheology in either of the models in this study; the fact that our modeling still captures the observed behaviors indicates micro-inertial effects are not a key mechanism in the observed behaviors. Similarly, the use of the NDPM model in case-1 separates out the origins of lift plateauing from the transition effects observed in later studies by Guillard et al.⁶² who observed similar reductions in both the force components upon continued rotation of cylinders in similar geometries. We believe later experimentally observed phenomena can be captured with the DPM model. We also emphasize that the continuum approach seems a more useful approach, compared to using grain-scale data, to determine further-reduced models of intrusion, due to the simplicity

of its large-scale characterization of systems. One such work on this front was done in Agarwal and Karsai et al.³¹, which develops a generalized, rate-dependent, dynamic resistive force theory (DRFT) for rapid intrusion of generic intruders. In the future, the work could be extended to three dimensions to extensively compare the computational advantage of using such methods.

Conflicts of interest

There are no conflicts to declare.

Acknowledgements

SA and KK acknowledge support from Army Research Office (ARO) grants W911NF1510196, W911NF1810118, and W911NF1910431. AK and DG acknowledge support from ARO grant W911NF-18-1-0120. We also acknowledge support from the U.S. Army’s Tank Automotive Research, Development, and Engineering Center (TARDEC) and thank Dr. Christian Hubicki for his support in conducting vertical intrusion experiments.

Notes and references

- 1 A. Soliman, S. Reid and W. Johnson, *International Journal of Mechanical Sciences*, 1976, **18**, 279–284.
- 2 M. Omidvar, M. Iskander and S. Bless, *International Journal of Impact Engineering*, 2014, **66**, 60–82.
- 3 D. Ortiz, N. Gravish and M. T. Tolley, *IEEE Robotics and Automation Letters*, 2019, **4**, 2630–2636.
- 4 D. Van Der Meer, *Annual review of fluid mechanics*, 2017, **49**, 463.
- 5 B. Andreotti, Y. Forterre and O. Pouliquen, *Granular media: between fluid and solid*, Cambridge University Press, 2013.
- 6 D. M. Wood, *Soil behaviour and critical state soil mechanics*, Cambridge University Press, 1990.
- 7 R. P. Jensen, P. J. Bosscher, M. E. Plesha and T. B. Edil, *International Journal for Numerical and Analytical Methods in Geomechanics*, 1999, **23**, 531–547.
- 8 R. P. Jensen, M. E. Plesha, T. B. Edil, P. J. Bosscher and N. B. Kahla, *International Journal of Geomechanics*, 2001, **1**, 21–39.
- 9 N. V. Brilliantov, F. Spahn, J.-M. Hertzsch and T. Pöschel, *Physical review E*, 1996, **53**, 5382.
- 10 L. E. Silbert, D. Ertaş, G. S. Grest, T. C. Halsey, D. Levine and S. J. Plimpton, *Physical Review E*, 2001, **64**, 051302.
- 11 K. Kamrin and G. Koval, *Physical Review Letters*, 2012, **108**, 178301.
- 12 S. Kim and K. Kamrin, *Physical Review Letters*, 2020, **125** (8), 088002.
- 13 D. Jajcevic, E. Siegmann, C. Radeke and J. G. Khinast, *Chemical Engineering Science*, 2013, **98**, 298–310.
- 14 W. Zhong, A. Yu, X. Liu, Z. Tong and H. Zhang, *Powder Technology*, 2016, **302**, 108–152.
- 15 C. Kelly, N. Olsen and D. Negrut, *Multibody Systems Dynamics*, 2020, **5**, 355–379.
- 16 N. Vriend, J. McElwaine, B. Sovilla, C. Keylock, M. Ash and P. Brennan, *Geophysical Research Letters*, 2013, **40**, 727–731.
- 17 K. E. Daniels and N. W. Hayman, *Journal of Geophysical Re-*

- search: *Solid Earth*, 2008, **113**, B11.
- 18 N. Mahabadi and J. Jang, *Applied Physics Letters*, 2017, **110**, 041907.
 - 19 N. V. Brilliantov and T. Pöschel, *Kinetic theory of granular gases*, Oxford University Press, 2010.
 - 20 J. T. Jenkins and M. Richman, *The Physics of fluids*, 1985, **28**, 3485–3494.
 - 21 A. Schofield and P. Wroth, *Critical state soil mechanics*, McGraw-hill, 1968.
 - 22 H.-S. Yu, Keynote lecture. Proc. 12th Int. Conf. IACMAG, Goa, India, 2008, pp. 361–378.
 - 23 P. Jop, Y. Forterre and O. Pouliquen, *Nature*, 2006, **441**, 727–730.
 - 24 J. Wiacek, M. Molenda, J. Horabik *et al.*, *Mechanical properties of granular agro-materials. Continuum and discrete approach*, Polska Akademia Nauk, 2011.
 - 25 D. L. Henann and K. Kamrin, *Proceedings of the National Academy of Sciences*, 2013, **110**, 6730–6735.
 - 26 K. Kamrin, *Frontiers in Physics*, 2019, **7**, 116.
 - 27 S. Dunatunga and K. Kamrin, *Journal of Fluid Mechanics*, 2015, **779**, 483–513.
 - 28 S. Agarwal, C. Senatore, T. Zhang, M. Kingsbury, K. Iagnemma, D. I. Goldman and K. Kamrin, *Journal of Terramechanics*, 2019, **85**, 1–14.
 - 29 C. Dávalos, J. Cante, J. Hernández and J. Oliver, *International Journal of Solids and Structures*, 2015, **71**, 99–125.
 - 30 C. Peng, X. Guo, W. Wu and Y. Wang, *Acta Geotechnica*, 2016, **11**, 1231–1247.
 - 31 S. Agarwal, A. Karsai, D. I. Goldman and K. Kamrin, *arXiv preprint arXiv:2005.10976*, 2020.
 - 32 S. Dunatunga and K. Kamrin, *Journal of the Mechanics and Physics of Solids*, 2017, **100**, 45–60.
 - 33 S. Agarwal, *Continuum Modeling of Granular Flows and Intrusions*, 2020, MATLAB Central File Exchange.
 - 34 D. Sulsky, Z. Chen and H. L. Schreyer, *Computer methods in applied mechanics and engineering*, 1994, **118**, 179–196.
 - 35 A. Jarray, H. Shi, B. J. Scheper, M. Habibi and S. Luding, *Scientific reports*, 2019, **9**, 1–12.
 - 36 J. Aguilar, T. Zhang, F. Qian, M. Kingsbury, B. McInroe, N. Mazouchova, C. Li, R. Maladen, C. Gong, M. Travers *et al.*, *Reports on Progress in Physics*, 2016, **79**, 110001.
 - 37 H. Li, Y. Lai, L. Wang, X. Yang, N. Jiang, L. Li, C. Wang and B. Yang, *Cold regions science and technology*, 2019, **157**, 171–186.
 - 38 X. Zhang, D. Sheng, G. P. Kouretzis, K. Krabbenhoft and S. W. Sloan, *Physical Review E*, 2015, **91**, 022204.
 - 39 F. Guillard, Y. Forterre and O. Pouliquen, *Physics of Fluids*, 2014, **26**, 043301.
 - 40 J. Wu, G. Kouretzis, L. Suwal, Y. Ansari and S. W. Sloan, *Canadian Geotechnical Journal*, 2020, **57**, 1472–1483.
 - 41 Y. Ding, N. Gravish and D. I. Goldman, *Physical review letters*, 2011, **106**, 028001.
 - 42 M. Klinkmüller, G. Schreurs, M. Rosenau and H. Kemnitz, *Tectonophysics*, 2016, **684**, 23–38.
 - 43 R. L. De La Cruz and G. Caballero-Robledo, *Journal of Fluid Mechanics*, 2016, **800**, 248–263.
 - 44 A. Merceron, A. Sauret and P. Jop, *EPL (Europhysics Letters)*, 2018, **121**, 34005.
 - 45 S. Pravin, B. Chang, E. Han, L. London, D. I. Goldman, H. M. Jaeger and S. T. Hsieh, *arXiv preprint arXiv:2010.15172*, 2020.
 - 46 L. K. Roth, E. Han and H. M. Jaeger, *arXiv preprint arXiv:1910.10358*, 2019.
 - 47 H. Katsuragi and D. J. Durian, *Nature physics*, 2007, **3**, 420–423.
 - 48 T. A. Brzinski III, P. Mayor and D. J. Durian, *Physical review letters*, 2013, **111**, 168002.
 - 49 W. Kang, Y. Feng, C. Liu and R. Blumenfeld, *Nature communications*, 2018, **9**, 1–9.
 - 50 V. V. Sokolovskii, *Statics of soil media*, Butterworths Scientific Publications, 1960.
 - 51 A. F. Bower, *Chapter 6, Applied mechanics of Solids*, CRC press, 2009.
 - 52 J. Aguilar and D. I. Goldman, *Nature Physics*, 2016, **12**, 278–283.
 - 53 L. Prandtl, *Nachr. Ges. Wiss. Göttingen*, 1920, 74–85.
 - 54 R. Hill, *The Quarterly Journal of Mechanics and Applied Mathematics*, 1949, **2**, 40–52.
 - 55 A. E. Minetti, G. Machtsiras and J. C. Masters, *Journal of biomechanics*, 2009, **42**, 2188–2190.
 - 56 N. Sidelnik and B. Young, *Sports Engineering*, 2006, **9**, 129–135.
 - 57 N. Gravish, P. B. Umbanhowar and D. I. Goldman, *Physical review letters*, 2010, **105**, 128301.
 - 58 M. Kobayakawa, S. Miyai, T. Tsuji and T. Tanaka, *Journal of Terramechanics*, 2020, **90**, 3–10.
 - 59 E. Kashizadeh, J. Hambleton and S. Stanier, Proc. 14th Int. Conf. IACMAG, Kyoto, Japan, 2015, pp. 159–164.
 - 60 Z. Jin, Z. Shi and J. Hambleton, *Spree Internal Report*, 2020, 20–7/495S.
 - 61 Y. Feng, R. Blumenfeld and C. Liu, *Soft matter*, 2019, **15**, 3008–3017.
 - 62 F. Guillard, Y. Forterre and O. Pouliquen, *Physical review letters*, 2013, **110**, 138303.